



MEaSURES (Making Earth System Data Records for Use in Research Environments) Geosynchronous Land Surface Temperature Product (GEO-LST) Algorithm Theoretical Basis Document

Kerry Cawse-Nicholson¹, Simon Hook¹, Glynn Hulley¹, Rachel Pinker²

¹Jet Propulsion Laboratory, California Institute of Technology

²University of Maryland

**National Aeronautics and
Space Administration**

**Jet Propulsion Laboratory
California Institute of Technology
Pasadena, California**

November 2019

This research was carried out at the Jet Propulsion Laboratory, California Institute of Technology, under a contract with the National Aeronautics and Space Administration.

Reference herein to any specific commercial product, process, or service by trade name, trademark, manufacturer, or otherwise, does not constitute or imply its endorsement by the United States Government or the Jet Propulsion Laboratory, California Institute of Technology.

© 2019. California Institute of Technology. Government sponsorship acknowledged.

Contacts

Kerry Cawse-Nicholson

MS 183-501

Jet Propulsion Laboratory

4800 Oak Grove Dr.

Pasadena, CA 91109

Email: kcawseni@jpl.nasa.gov

Office: (818) 354-1594

Contents

Contacts	2
1 Introduction	4
2 GOES Background	6
3 Thermal Infrared Radiative Transfer	8
3.1 Thermal Infrared Radiance.....	8
4 Method	11
4.1 LST Retrieval	12
4.2 Radiative Transfer Model	14
4.3 Atmospheric Profiles	17
4.3.1 MERRA-2	17
4.4 Emissivity.....	19
5 Uncertainty Analysis	21
5.1 The Temperature and Emissivity Uncertainty Simulator	21
5.2 Atmospheric Profiles	22
5.3 Radiative Transfer Model	22
5.4 Surface End-Member Selection.....	22
5.5 Radiative Transfer Simulations	23
5.6 Error Propagation	25
5.7 Parameterization of Uncertainties	26
6 Validation	28
7 References	32

1 Introduction

This document outlines the theory and methodology for generating the MEaSUREs (Making Earth System Data Records for Use in Research Environments) Land Surface Temperature (LST) product derived from the Geostationary Operational Satellite (GOES) satellite data record. The GEO-LST product will include LST produced hourly over North and South America for GOES-8 through GOES-15 satellites since 2000. This is version 1.0 of the ATBD and the goal is maintaining a ‘living’ version of this document with changes made when necessary.

Land Surface Temperature and Emissivity (LST&E) are critical variables used in a wide range of Earth science studies. They are necessary inputs for surface energy balance models used in drought monitoring, soil moisture estimation, and monitoring water consumptive use (Anderson et al. 2011a; Hain et al. 2011; Semmens et al. 2016). They are used for the retrieval of climate variables such as tropospheric water vapor and air temperature (Seemann et al. 2008; Susskind and Blaisdell 2008; Yao et al. 2011). They are also used to monitor climate warming trends (Hall et al. 2012; Schneider and Hook 2010), measure the urban heat island effect (Dousset and Gourmelon 2003; Luvall et al. 2015) and heat waves (Dousset et al. 2011; Luvall et al. 2015), detect land cover and land use change (French et al. 2008; Hulley et al. 2014a), and map surface composition (Hook et al. 2005; Vaughan et al. 2005).

NASA has identified LST&E data as an important Earth System Data Record (ESDR) (NASA 2005, 2011) along with other international organizations (e.g. Global Climate Observing System (GCOS), 2003; Climate Change Science Program (CCSP), 2006). LST was recently designated as an Essential Climate Variable (ECV) by GCOS and several international initiatives have been established to utilize LST&E data including the EarthTemp network (<http://www.earthtemp.net/>), GlobTemperature (<http://www.globtemperature.info/>) and the International Land Surface Temperature and Emissivity Working Group (ILSTE-WG, <http://ilste-wg.org/>).

LST&E products are routinely produced by NASA and NOAA from sensors in low earth orbit (LEO) from the Moderate Resolution Imaging Spectroradiometer (MODIS) and Visible Infrared Imaging Radiometer Suite (VIIRS) sensors on board the Aqua (2002)/Terra (2000) and Suomi-NPP (2011) platforms respectively. LST products are also produced from sensors in geostationary Earth

orbit (GEO) such as the Geostationary Operational Environmental Satellites (GOES). Sensors in LEO orbits provide global coverage at moderate spatial resolutions (~1km) but more limited temporal coverage (up to twice-daily), while sensors in GEO orbits provide more frequent measurements (hourly) at lower spatial resolutions (~2-4 km) over a geographically restricted area. For example, the GOES sensors produce data over North America every 15 minutes and South America every 3 hours. These sensor-based LST&E products, however, are generated with varying accuracies depending on the input data. These input data include ancillary data such as atmospheric water vapor and algorithmic approaches. They are also on different space-time grids and lack full uncertainty information limiting their usefulness for many studies. Our current project was selected to address these limitations by creating a set of unified and coherent LST&E products and this follow-on work will develop and extend these products. LST&E data are used for many Earth surface related studies such as surface energy balance modeling (Zhou et al. 2003b) and land-cover land-use change detection (French et al. 2008), while they are also critical for accurately retrieving important climate variables such as air temperature and relative humidity (Yao et al. 2011). The LST is an important long-term climate indicator, and a key variable for drought monitoring over arid lands (Anderson et al. 2011a; Rhee et al. 2010). The LST is an input to ecological models that determine important variables used for water use management such as evapotranspiration and soil moisture (Anderson et al. 2011b).

GEO LST products produced from GOES are currently available through NOAA OSPO (<http://www.ospo.noaa.gov/Products/land/glst/>) but are produced using different retrieval algorithms throughout the GOES record, e.g. GOES sensors 8-11 use a split-window algorithm, while GOES sensors 12-14 use a single channel algorithm (since the 11-12 micron band combination necessary for the split-window was not available for these sensors). This results in a discontinuity in the retrieval record and affects the accuracy of the GOES LST time series beginning with GOES 12. To address this issue, we developed a GEO-LST product using a consistent single-channel GOES algorithm applicable to all GOES sensors from GOES 8-16 and onward. The algorithm uses a radiative transfer approach for the atmospheric correction similar to the MxD21 approach, combined with an improved Combined ASTER and MODIS Emissivity for Land (CAMEL) emissivity data record for the emissivity correction

(<https://lpdaac.usgs.gov/products/cam5k30emv002/>). **The GEO-LST product merges six generations of GOES sensors and instrument characteristics.**

2 GOES Background

The Geostationary Operational Environment Satellite (GOES) system is operated by the National Oceanic and Atmospheric Administration, National Environmental Satellite, Data and Information Service (NESDIS). The GOES system is mounted on a satellite operating at an orbit of 35,790 km above the earth, remaining stationary to a given point on the ground. The GOES provides data at high temporal frequency (5 minutes) with continental-scale coverage (N. and S. America). In this study observations from GOES-08 - GOES-15 (2000 – 2016) will be utilized [Table 1]. Typically, the GOES imager includes five spectral channels (one visible, four infrared). For GOES 8-10 the channels are located at 3.9, 6.75, 10.7, and 12.2 μm , whereas for GOES 11-15, the 6.75 μm channel was moved to 6.5 μm and the 12 μm channel was moved to 13.3 μm . The visible, mid-infrared and 11 μm band are typically used for cloud screening while the two thermal infra-red (TIR) bands (10.2-11.2 μm and 11.5-12.5 μm) are used in what is known as a “split-window” approach to retrieve LST.

Over the period of this study, two separate operational GOES Imagers, one located at a longitude of -75° E (referred to as GOES-East) and one located at a longitude of 135° W (referred to as GOES-West) continuously provided imagery over North and South America. The temporal sampling of the GOES Imager is every hour in “Northern Hemisphere Extended” mode, which covers North America, as well as parts of South America, as seen in Figure 1. Spectral distribution of the GOES 8-15 series are provided in NOAA NESDIS STAR GOES Imager LST ATBD (Version 3.0).

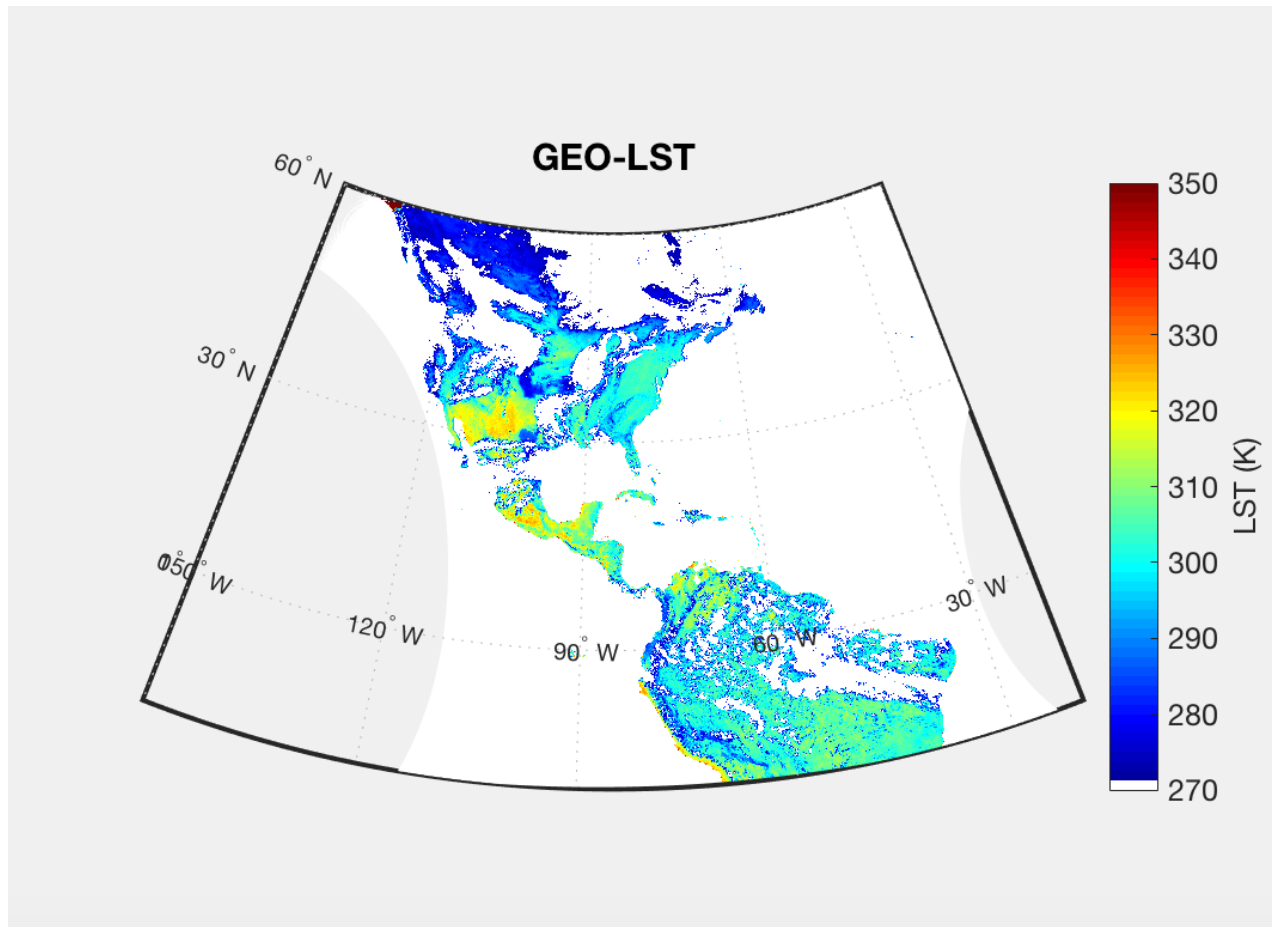


Figure 1: A sample a cloud-screened GEO-LST image acquired on 4/28/2003 at 1815UTC.

3 Thermal Infrared Radiative Transfer

3.1 Thermal Infrared Radiance

As described in (Hulley et al., 2016), the at-sensor measured radiance in the TIR spectral region (7–14 μm) is a combination of three primary terms: the Earth-emitted radiance, reflected downwelling sky irradiance, and atmospheric path radiance. The Earth-emitted radiance is a function of temperature and emissivity and gets attenuated by the atmosphere on its path to the satellite. The atmosphere also emits radiation, some of which reaches the sensor directly as “path radiance,” while some gets radiated to the surface (irradiance) and reflected back to the sensor, commonly known as the reflected downwelling sky irradiance. Reflected solar radiation in the TIR region is negligible (Figure 1) and a much smaller component than the surface-emitted radiance. One effect of the sky irradiance is the reduction of the spectral contrast of the emitted radiance, due to Kirchhoff’s law. Assuming the spectral variation in emissivity is small (Lambertian assumption), and using Kirchhoff’s law to express the hemispherical-directional reflectance as directional emissivity ($\rho_\lambda = 1 - \epsilon_\lambda$), the clear-sky at-sensor radiance can be written as three terms: the Earth-emitted radiance described by Planck’s function and reduced by the emissivity factor, ϵ_λ ; the reflected downwelling irradiance; and the path radiance.

$$L_\lambda(\theta) = [\epsilon_\lambda B_\lambda(T_s) + (1 - \epsilon_\lambda)L_\lambda^\downarrow]\tau_\lambda(\theta) + L_\lambda^\uparrow(\theta) \quad (1)$$

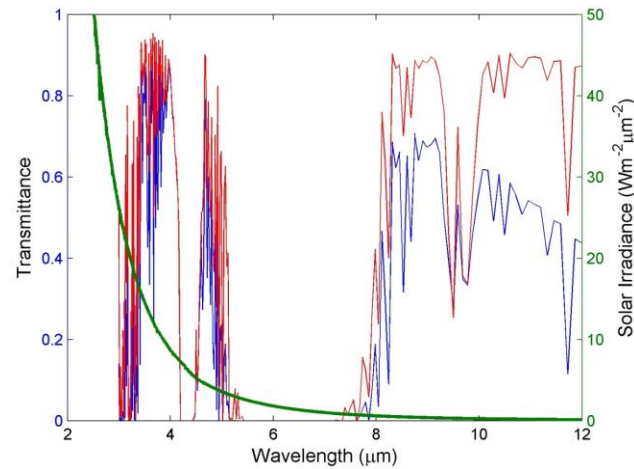


Figure 2. Simulated atmospheric transmittance for a US Standard Atmosphere (red) and tropical atmosphere (blue) in the 3–12 μm region. Also shown is the solar irradiance contribution $\text{W/m}^2/\mu\text{m}^2$ (Hulley et al., 2016).

Where:

$L_\lambda(\theta)$ = at-sensor radiance;

λ = wavelength;

θ = observation angle;

ϵ_λ = surface emissivity;

T_s = surface temperature;

L_λ^\downarrow = downwelling sky irradiance;

$\tau_\lambda(\theta)$ = atmospheric transmittance;

$L_\lambda^\uparrow(\theta)$ = atmospheric path radiance

$B_\lambda(T_s)$ = Planck function, described by Planck's law:

$$B_\lambda = \frac{c_1}{\pi\lambda^5} \left(\frac{1}{\exp\left(\frac{c_2}{\lambda T}\right) - 1} \right) \quad (2)$$

$c_1 = 2\pi hc^2 = 3.74 \cdot 10^{-16} \text{ W}\cdot\text{m}^2$ (1st radiation constant)

$h = 6.63 \cdot 10^{-34} \text{ W}\cdot\text{s}^2$ (Planck's constant)

$c_2 = h\cdot c/k = 1.44 \times 10^4 \text{ }\mu\text{m}\cdot\text{K}$ (2nd radiation constant)

$k = 1.38 \times 10^{-23} \text{ W}\cdot\text{s}\cdot\text{K}^{-1}$ (Boltzmann's constant)

$c = 2.99 \cdot 10^8 \text{ m}\cdot\text{s}^{-1}$ (speed of light)

Equation (1) gives the at-sensor radiance for a single wavelength λ , while the measurement from a sensor is typically measured over a range of wavelengths, or band. The at-sensor radiance for a discrete band i , is obtained by weighting and normalizing the at-sensor spectral radiance calculated by Equation (1) with the sensor's spectral response function for each band, Sr_λ , as follows:

$$L_i(\theta) = \frac{\int Sr_\lambda(i) \cdot L_\lambda(\theta) \cdot d\lambda}{Sr_\lambda(i) \cdot d\lambda} \quad (3)$$

Using Equations (1) and (3), the surface radiance for band i can be written as a combination of two terms: Earth-emitted radiance, and reflected downward irradiance from the sky and surroundings:

$$L_{s,i} = \epsilon_i B_i(T_s) + (1 - \epsilon_i) L_i^\downarrow = \frac{L_i(\theta) - L_i^\uparrow(\theta)}{\tau_i(\theta)} \quad (4)$$

The atmospheric parameters, L_λ^\downarrow , $\tau_\lambda(\theta)$, $L_\lambda^\uparrow(\theta)$, are estimated with a radiative transfer model such as RTTOV or MODTRAN (Kneizys et al. 1996) discussed in the next section, using input atmospheric fields of air temperature, relative humidity, and geopotential height.

4 Method

Figure 2 shows that GOES radiance data for the 11 μm band are first atmospherically corrected using the Radiative Transfer for TOVS (RTTOV), which is a computationally efficient radiative transfer model applicable to a variety of sensors and wavelength ranges (Saunders et al. 1999). The model has been validated against IASI, and is efficient for full scale retrievals (Matricardi 2009). RTTOV v12 is the latest version, and was used in the processing of the GOES radiance images.

Given an atmospheric profile of temperature, water vapor and optionally other trace gases together with view angle geometry, RTTOV will compute the atmospheric transmittance and path radiances required for atmospheric correction in each of the channels of the sensor being simulated.

Numerical Weather Prediction (NWP) models use current weather conditions, observed from various sources (e.g., radiosondes, surface observations, and weather satellites) as input to dynamic mathematical models of the atmosphere to predict the weather. The Modern Era Retrospective-analysis for Research and Applications (MERRA) product provided by the Goddard Earth Observing System Data Assimilation System Version 5.2.0 (GEOS-5.2.0) produces near-real time atmospheric products, which are used as input to RTTOV to perform the atmospheric correction. The MERRA profiles are first interpolated in time to the GOES observation using the [00 06 12 18] UTC analysis observation hours before input into RTTOV.

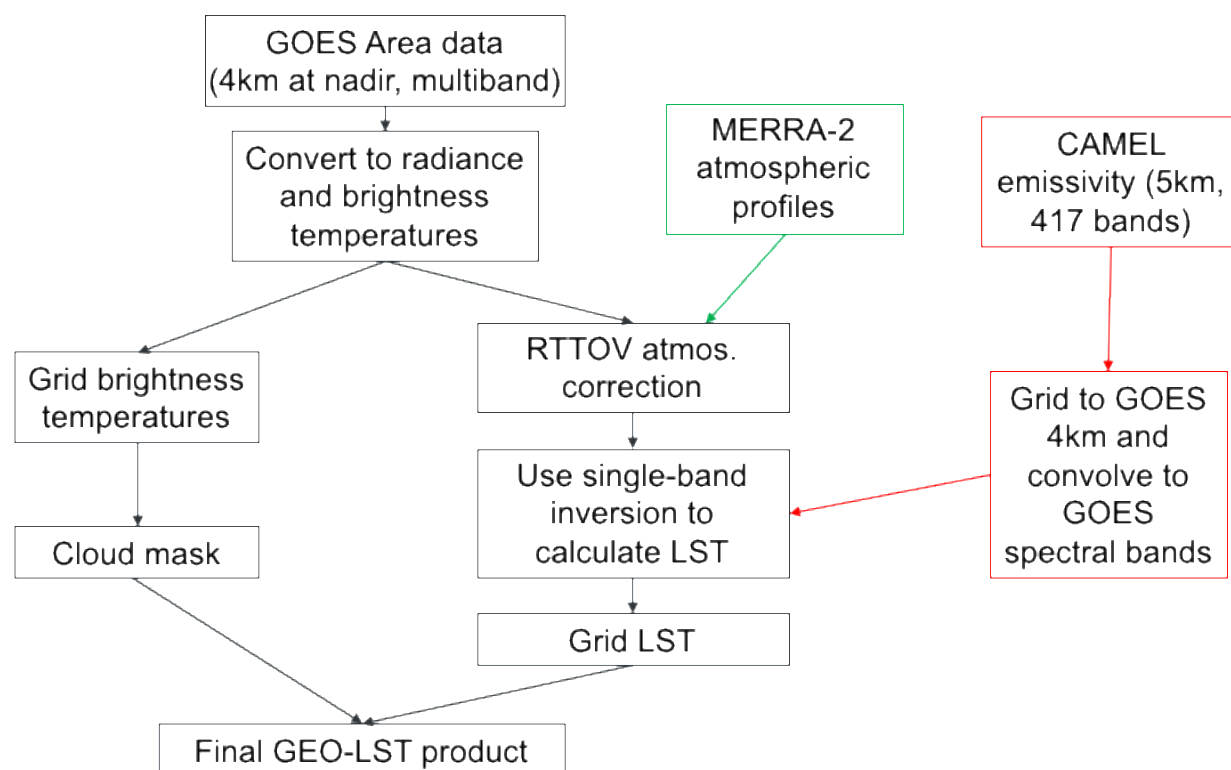


Figure 2: GOES data is converted to radiance and brightness temperature, and then processed for LST and cloud masks. The LST algorithm uses RTTOV and MERRA-2 data for atmospheric correction and accepts CAMEL emissivity as input.

4.1 LST Retrieval

GOES radiance data are available from the CLASS servers (www.class.ncdc.noaa.gov) in GVAR format, which is converted to radiance using the scaling described in Weinreb et al. (1997). The observed radiances are then atmospherically corrected using RTTOV with input from MERRA-2, as described above, and corrected for emissivity using the CAMEL ESDR rescaled and spectrally adjusted to GOES spatial resolution and bandpass. Once the surface emitted radiance is determined, the LST can be retrieved by simply inverting

the Planck function and using a look-up-table approach to convert radiance into temperature. Theoretically, any band used should retrieve the same temperature, but uncertainties in the atmospheric correction will result in subtle differences as different bands have stronger atmospheric absorption features than others that may be imperfectly corrected for atmospheric absorption. For example, a band near 8 μm will have larger dependence on water vapor, while the 9–10- μm region will be more susceptible to ozone absorption. Jimenez-Munoz and Sobrino (2010) applied this method to ASTER data by using atmospheric functions (AFs) to account for atmospheric effects. The AFs can be computed by the radiative transfer equation or empirically given the total water vapor content. The clearest ASTER band (13 or 14) was used to retrieve the temperature, with the emissivity determined using a normalized difference vegetation index (NDVI) fractional vegetation cover approach. A similar procedure has been proposed to retrieve temperatures from the Landsat TIR band 6 on ETM+ and TM sensors (Li et al. 2004). Because of the changes in band designations across the GOES time series, we use a single band inversion on Band 4 in the 11 micron window region to generate the GEO-LST product, as done in Malakar et al. (2018). As in (Hulley et al., 2016), from eq. 4 we can rearrange terms to compute the surface emitted radiance:

$$L_s = B(T_s) = \frac{\frac{L - L^\uparrow}{\tau} - (1 - \epsilon) L^\downarrow}{\epsilon} \quad (5)$$

where $B(T_s)$ is the Planck function at temperature T_s :

$$B(T_s) = \frac{c_1 \lambda^{-5}}{\left(e^{\frac{c_2}{\lambda T_s}} - 1 \right)} \quad (6)$$

where $c_1 = 1.19 \times 10^{-16} \text{ W m}^{-2} \text{ sr}^{-1}$, and $c_2 = 1.44 \times 10^4 \mu\text{m K}$.

The surface temperature can then be retrieved by inverting the Planck function with the emitted radiance as follows:

$$T_s = \frac{c_2}{\lambda_c \ln \left(1 + \frac{c_1 \lambda_c^{-5}}{L_s} \right)} \quad (7)$$

where T_s is the retrieved LST, and λ_c is the sensor's central wavelength equivalent to a delta function response. This formulation, however, will become increasingly inaccurate for a sensor's spectral response that deviates from delta function behavior. Instead we use a look up table (LUT) approach to compute expected radiances for each respective GOES sensors' spectral response over a range of temperatures in 0.01 K intervals that encompass the full range of expected Earth-like temperatures (typically 150 to 380 K). This results in a table of radiance versus temperature values for each given sensor. The table can then simply be 'inverted' by interpolating to get the retrieved temperature (LST), given the estimated surface emitted radiance.

4.2 Radiative Transfer Model

With the next generation's state-of-the-art, mid- and long-wave infrared (IR) hyperspectral sensors due for launch in the next decade, there has been greater demand for higher resolution and quality radiative transfer modeling. The current choice of radiative transfer model for atmospherically correcting GOES TIR data is the latest version of the radiative transfer model called RTTOV. It is a very fast radiative transfer model for nadir-viewing passive visible, infrared and microwave satellite radiometers, spectrometers and interferometers (Saunders et al. 1999). RTOV is written in FORTRAN-90 code, for simulating satellite radiances, designed to be incorporated within users' applications. RTTOV was originally developed at ECMWF in the early 90's for TOVS (Eyre and Woolf 1988). Subsequently, the original code has gone through several developments (Matricardi et al. 2001; Saunders et al. 1999), more recently within the EUMETSAT NWP Satellite Application Facility (SAF), of which RTTOV v11 is the latest version. It is actively

developed by ECMWF and UK Met Office. RTTOV has been sufficiently tested and validated and is conveniently fast for full scale retrievals (Matricardi 2009). A number of satellite sensors are supported from various platforms (e.g. https://nwpsaf.eu/deliverables/rtm/rttov_description.html). Given an atmospheric profile of temperature, water vapor and optionally other trace gases (for example ozone and carbon dioxide) together with satellite and solar zenith angles and surface temperature, pressure and optionally surface emissivity and reflectance, RTTOV will compute the top of atmosphere radiances in each of the channels of the sensor being simulated. Users can also specify the selected channels to be simulated. Mathematically, in vector notation, given a state vector, \mathbf{x} , which describes the atmospheric/surface state as a profile and surface variables the radiance vector, \mathbf{y} , for all the channels required to be simulated is given by (Saunders et al. 1999):

$$\mathbf{y} = H(\mathbf{x}) \tag{8}$$

Where H is the radiative transfer model, i.e. RTTOV (also referred to as the observation operator in data assimilation parlance). This is known as the 'direct' or 'forward' model.

An important feature of the RTTOV model is that it not only performs the fast computation of the forward (or direct) clear-sky radiances but also the fast computation of the gradient of the radiances with respect to the state vector variables for the input state vector values. The Jacobian matrix \mathbf{H} which gives the change in radiance $\delta\mathbf{y}$ for a change in any element of the state vector $\delta\mathbf{x}$ assuming a linear relationship about a given atmospheric state \mathbf{x}_0 :

$$\Delta\mathbf{y} = \mathbf{H}(\mathbf{x}_0)\delta\mathbf{x} \tag{9}$$

The elements of \mathbf{H} contain the partial derivatives $\frac{\partial y_i}{\partial x_j} \left(\frac{dy_i}{dx_j} \right)$ where the subscript i refers to channel number and j to position in state vector.

The Jacobian gives the top of atmosphere radiance change for each channel from each level in the profile given a unit perturbation at any level of the profile vectors or in any of the surface/cloud parameters. It shows clearly, for a given profile, which levels in the atmosphere are most sensitive to changes in temperature and variable gas concentrations for each channel.

In RTTOV the transmittances of the atmospheric gases are expressed as a function of profile dependent predictors. This parameterization of the transmittances makes the model computationally efficient. The RTTOV fast transmittance scheme uses regression coefficients derived from accurate Line by Line computations to express the optical depths as a linear combination of profile dependent predictors that are functions of temperature, absorber amount, pressure and viewing angle (Matricardi and Saunders, 1999). The regression coefficients are computed using a training set of diverse atmospheric profiles chosen to represent the range of variations in temperature and absorber amount found in the atmosphere (Matricardi and Saunders, 1999; Chevallier, 2000; and Matricardi, 2008, 2009). The selection of the predictors is made according to the coefficients file supplied to the program.

Table 1: Geophysical data available in the MERRA analysis product. Columns under Mandatory specify if the variables is needed for determining atmospheric correction parameters. Data are output in 6hr analysis for 42 pressure levels at 0.5 degree x 0.625 degree spatial resolution.

MERRA Analysis Data (inst6_3d_ana_Np)				
Geophysical fields		Required?	Available?	Remarks
time	Time	Yes	Yes	
lat	Latitude	Yes	Yes	
lon	Longitude	Yes	Yes	
nlev	nLevel	Yes	Yes	
p	Pressure	Yes	Yes	
t	Air Temperature	Yes	Yes	
q	Specific Humidity	Yes	Yes	
sp	Surface Pressure	Yes	Yes	
skt	Surface Temperature	Yes	No	T value at the first valid level above surface is used.
t2	Temperature at 2 m	Yes	No	T value at the first valid level above surface is used

q2	Specific Humidity at 2 m	Yes	No	Q value at the first valid level above surface is used
ism	Land Sea Mask	Yes	No	Auxiliary database
el	Elevation	Yes	No	Auxiliary database

4.3 Atmospheric Profiles

4.3.1 MERRA-2

MERRA-2 is a follow-on product to the original MERRA project for the modern satellite era (1979-2015). It has been expanded to use new observations including GOES, MODIS, AVHRR, GPS Radio Occultation, OMI, and MLS. The latest enhancement includes improved water vapor assimilation resulting in a balance between precipitation and evaporation. Consequentially, one of the major advancements is the addition of land surface forcing by observed precipitation. The GEO-LST algorithm uses the MERRA-2 analysis data for its standard atmospheric correction. MERRA-2 data are output in 6hr analysis for 42 pressure levels at 0.5 degree x 0.625 degree spatial resolution. The MERRA-2 profiles are first interpolated in time to the GOES observation using the [00 06 12 18Z] analysis observation hours before ingesting into RTTOV. Table 1 shows MERRA-2 geophysical data available in the MERRA-2 analysis product and the variables required for the input data into RTTOV for the atmospheric correction.

Table 2: Geophysical data available in the NCEP GFS analysis product. Columns under Mandatory specify if the variables is needed for determining atmospheric correction parameters. Data are output in 3hr analysis for 26 pressure levels at 0.5 degree spatial resolution.

NCEP GSF Data (NCEP-GFS-03HR-ANC)				
Geophysical fields		Required?	Available?	Remarks
time	Time	Yes	Yes	
lat	Latitude	Yes	Yes	
lon	Longitude	Yes	Yes	

MEASURES GEO-LAND SURFACE TEMPERATURE ATBD

nlev	nLevel	Yes	Yes	
p	Pressure	Yes	Yes	
t	Air Temperature	Yes	Yes	
q	Specific Humidity	Yes	Yes	
sp	Surface Pressure	Yes	Yes	
skt	Surface Temperature	Yes	Yes	
t2	Temperature at 2 m	Yes	No	T value at the first valid level above surface is used
q2	Specific Humidity at 2 m	Yes	No	Q value at the first valid level above surface is used
ism	Land Sea Mask	Yes	No	Auxiliary database
el	Elevation	Yes	No	Auxiliary database

The RTTOV output data of transmittance, path radiance, and sky irradiance are then gridded to the GOES swath at 4-km resolution using a bicubic interpolation approach. It should be noted that the data interpolation could potentially introduce errors, especially in humid regions where atmospheric water vapor can vary on smaller spatial scales than the native resolution of the input MERRA data at 0.5°. The propagation of these atmospheric correction errors would result in band-dependent surface radiance errors in both spectral shape and magnitude, which in turn could result in errors of retrieved Level-2 products such as surface emissivity and temperature. This is one of the main reasons that we implemented a Water Vapor Scaling (WVS) approach to help mitigate these errors.

4.4 Emissivity

The CAMEL emissivity product is generated by combining the MODIS UWBF and ASTER GEDv4 emissivity products, each produced by different methods/algorithms. The total uncertainty (see Figure 3) comprises 3 independent components of variability—a temporal, spatial, and algorithm variability. Each measure of uncertainty is provided for all 13 channels and every latitude-longitude point. A quality flag is provided for the total uncertainty as 0 if the pixel is over the sea or no CAMEL data is available, 1 if it is good quality data and 2 if the uncertainty values are unphysical. The total uncertainty is calculated as a root square sum of the three components. The spatial uncertainty component is calculated as the standard deviation of the surrounding 5x5 pixel emissivity, which is equivalent to a $0.25^{\circ} \times 0.25^{\circ}$ latitude-longitude region. This uncertainty represents the variability of the surrounding landscape (ocean is not included) and is only provided where the CAMEL emissivity quality flag is not zero. The temporal uncertainty is defined by the standard deviation of the 3 surrounding months (e.g. Oct. uncertainty = standard deviation (Sept., Oct., Nov.)) Algorithm uncertainty is

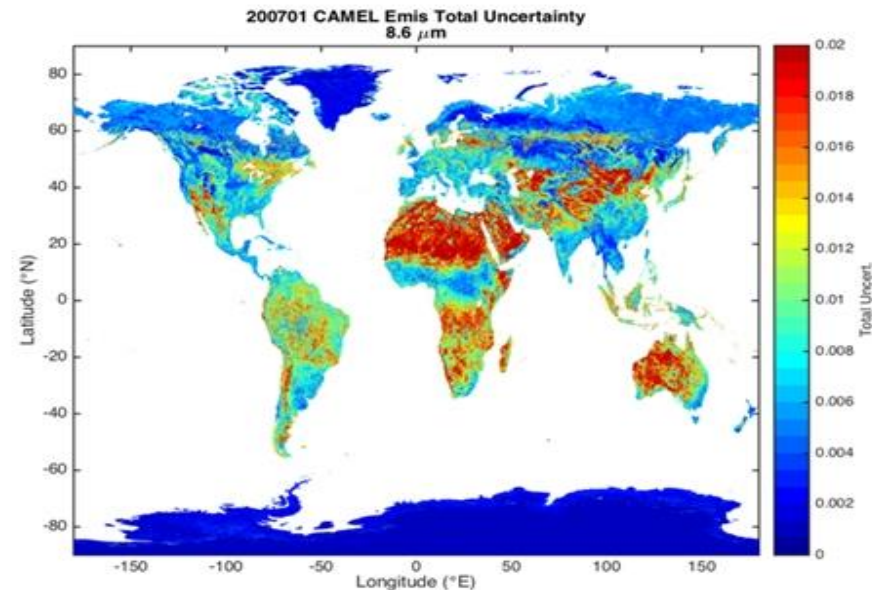


Figure 3: Total CAMEL emissivity uncertainty for January 2007 for the CAMEL emissivity 8.6 micron channel. The total uncertainty includes both spatial, temporal and algorithmic components.

estimated by the differences between the two CAMEL emissivity inputs: the ASTER GEDv4 and UWBF MODIS products. The CAMEL User Guide (Borbas et al., 2017) details the ASTER, and UWBF channel wavelengths, the method for combining the ASTER and UWBF emissivity to create the CAMEL product, and the method for determining the CAMEL emissivity algorithm uncertainty.

5 Uncertainty Analysis

NASA has identified a major need to develop long-term, consistent products valid across multiple missions, with well-defined uncertainty statistics addressing specific Earth-science questions. These products are termed Earth System Data Records (ESDRs), and LST&E has been identified as an important ESDR. Currently a lack of understanding of LST&E uncertainties limits their usefulness in land surface and climate models. In this section we present results from an LST&E uncertainty simulator that has been developed to quantify and model uncertainties for a variety of TIR sensors and LST algorithms (Hulley et al. 2012). Using the simulator, uncertainties were estimated for the GEO-LST product, including WVS. These uncertainties are parameterized according to view angle and estimated total column water vapor for application to real GOES data.

5.1 The Temperature and Emissivity Uncertainty Simulator

A Temperature Emissivity Uncertainty Simulator (TEUSim) has been developed for simulating LST&E uncertainties from various sources of error for the TES and SW algorithms in a rigorous manner for any appropriate TIR sensor. These include random errors (noise), systematic errors (calibration), and spatio-temporally correlated errors (atmospheric). The MODTRAN 5.2 radiative transfer model is used for the simulations with a global set of radiosonde profiles and surface emissivity spectra representing a broad range of atmospheric conditions and a wide variety of surface types. This approach allows the retrieval algorithm to be easily evaluated under realistic but challenging combinations of surface/atmospheric conditions. The TEUSim is designed to separately quantify error contributions from the following potential sources:

- Noise
- Model
- Atmospheric correction
- Undetected cloud
- Calibration

The results presented in this study will focus on the first three of these error sources: noise, model, and atmosphere.

5.2 Atmospheric Profiles

The TEUSim uses a global set of atmospheric radiosoundings constructed from the University of Wyoming Atmospheric Science Department's CLAR database (Galve et al. 2008). CLAR contains 382 globally distributed radiosoundings for both day and night in 65 layers from the surface to 100 km. The CLAR database includes a wide range of TCW estimates up to 7 cm and surface air temperature ranging from -20° C to 40° C. Radiosondes acquired from 2003 to 2006 were distributed over three latitude ranges (40% from 0° – 30° , 40% from 30° – 60° , 20% above 60°) and screened for cloud and fog contamination using a procedure described by Francois et al. (2002).

5.3 Radiative Transfer Model

In TEUSim the latest version of MODTRAN (v5.2) was used for the radiative transfer calculations. MODTRAN 5.2 uses an improved molecular band model, termed the Spectrally Enhanced Resolution MODTRAN (SERTRAN), which has a much finer spectroscopy (0.1 cm^{-1}) than previous versions ($1\text{--}2\text{ cm}^{-1}$). This results in higher accuracy in modeling of band absorption features in the longwave TIR window regions, and comparisons with line-by-line models has shown good accuracy (Berk et al. 2005).

5.4 Surface End-Member Selection

A selection of emissivity spectra from the ASTER Spectral Library v2.0 (ASTlib) (Baldrige et al. 2009a) were used to define the surface spectral emission term in MODTRAN. A total of 59 spectra were chosen based on certain criteria and grouped into four surface classifications: rocks (20), soils (26), sands (9), and graybodies (4). The doublets between $8\text{--}9.5\text{ }\mu\text{m}$ and $12.5\text{--}13\text{ }\mu\text{m}$ are the result of Si-O stretching, and the exact position of the feature at $11.2\text{ }\mu\text{m}$ is dependent on the size of the cation paired with the carbonate (CO_3) molecule. Spectra were chosen to represent the most realistic effective emissivities observed at the remote sensing scales of ASTER (90 m) and GOES (4 km) using the following methodology.

For rocks, certain spectra were removed prior to processing based on two considerations. First, samples that rarely exist as kilometer-scale, sub-aerial end-member exposures on the Earth's surface such as pyroxenite or serpentinite were eliminated. Second, and in parallel, spectrally similar samples were eliminated. Spectral similarity was defined by the location, shape, and magnitude of spectral features between 7 and 13 μm . All eliminated samples are represented in the final selection through spectrally-similar end-member types. The final rock set included 20 spectra.

ASTlib includes 49 soil spectra classified according to their taxonomy, such as Alfisol (9), Aridisol (14), Entisol (10), Inceptisol (7) and Mollisol (9). Filtering in this case was based solely on spectral similarity between each taxonomy type. The final soils set included 26 soil spectra.

A set of nine emissivity spectra collected in separate field campaigns during 2008 over large homogeneous sand dune sites in the southwestern United States in support of validation for the NAALSED v2.0 (Hulley et al. 2009b) were used for sands. The sand samples consist of a wide variety of different minerals including quartz, magnetite, feldspars, gypsum, and basalt mixed in various amounts, and represent a broad range of emissivities in the TIR as detailed in Hulley et al. (2009b).

To represent graybody surfaces, spectra of distilled water, ice, snow, and conifer were chosen from ASTlib. Four spectra were sufficient to represent this class since graybody surfaces exhibit low contrast and high emissivities. It should be noted that certain types of man-made materials were not included, such as aluminum roofs that do not occur at the spatial resolution of these sensors but should be included for higher-spatial-resolution data sets such as those provided by airborne instruments.

5.5 Radiative Transfer Simulations

In the TEUSim, each CLAR radiosonde profile for each set of end-member spectra was used as an input to MODTRAN 5.2. A seasonal rural aerosol was assumed with standard profiles for fixed gases within MODTRAN. For GOES, five viewing angles were used, representing the Gaussian angles proposed by Wan and Dozier (1996): 0° , 11.6° , 26.1° , 40.3° , and 53.7° . In the WVS simulation model, the downward sky irradiance, $L_\lambda(\theta)$, can be modeled using the path radiance, transmittance, and view angle. To simulate the downward sky irradiance in MODTRAN, the sensor target is placed a few meters above the surface, with surface emission set to zero,

and view angle set at the prescribed angles above. In this configuration, the reflected downwelling sky irradiance is estimated for a given view angle. The total sky irradiance contribution for band i is then calculated by summing the contribution of all view angles over the entire hemisphere:

$$L_i^\downarrow = \int_0^{2\pi} \int_0^{\pi/2} L_i^\downarrow(\theta) \cdot \sin\theta \cdot \cos\theta \cdot d\theta \cdot d\delta \quad (10)$$

where θ is the view angle and δ is the azimuth angle. To minimize computational time, the downward sky irradiance is first modeled as a non-linear function of path radiance at nadir view using (1) (Tonooka 2001):

$$L_i^\downarrow(\gamma) = a_i + b_i \cdot L_i^\uparrow(0, \gamma) + c_i L_i^\uparrow(0, \gamma)^2 \quad (11)$$

where a_i , b_i , and c_i are regression coefficients, and $L_i^\uparrow(0, \gamma)$ is computed by:

$$L_i^\uparrow(0, \gamma) = L_i^\uparrow(\theta, \gamma) \cdot \frac{1 - \tau_i(\theta, \gamma)^{\cos\theta}}{1 - \tau_i(\theta, \gamma)} \quad (12)$$

Equations (27) and (28) were used to estimate the downwelling sky irradiance in the TEUSim results using pre-calculated regression coefficients for GOES band 4. The reflected sky irradiance term is generally smaller in magnitude than the surface-emitted radiance, but needs to be taken into account, particularly on humid days when the total atmospheric water vapor content is high. The simulated LST is based on the surface air temperature in the CLAR database as follows:

$$LST_{sim} = T_{air} + \delta T \quad (13)$$

where LST_{sim} and T_{air} are the simulated LST and surface air temperature. Galve et al. (2008) found a mean δT of +3 K and standard deviation of 9 K from a global study of surface-air temperature differences over land in the MODIS MOD08 and MOD11 products. We therefore defined δT as a random distribution with a mean of 3 K and a standard deviation of 9 K for each profile input to MODTRAN.

A full LST retrieval requires atmospheric transmittance $\tau_\lambda(\theta)$, TOA radiance $L_\lambda(\theta)$, path radiance $L_\lambda^\uparrow(\theta)$, and downward sky irradiance $L_\lambda^\downarrow(\theta)$. To calculate the various sources of error in LST retrievals, these variables were simulated for the following conditions:

1. Perfect atmosphere (i.e., exact inputs): $L_\lambda(\theta)$ and atmospheric parameters $\tau_\lambda(\theta)$, $L_\lambda^\uparrow(\theta)$, and $L_\lambda^\downarrow(\theta)$ calculated using a given profile, surface type and viewing angle;
2. $L_\lambda(\theta)$ and adjusted atmosphere (i.e., imperfect inputs): $\tau'_\lambda(\theta)$, $L_\lambda^\uparrow(\theta)$, and $L_\lambda^\downarrow(\theta)$ calculated using perturbed temperature and humidity profiles to simulate real input data;

The above conditions were run for ‘perfect’ $L_\lambda(\theta)$ and also with adding random noise to the radiances based on the sensor’s noise equivalent delta temperature NE Δ T.

5.6 Error Propagation

The total LST uncertainty is based on model, atmospheric and measurement noise contributions can be written as:

$$\delta LST_{TES} = [\delta LST_M + \delta LST_A + \delta LST_N]^{1/2} \quad (14)$$

where δLST_M is the model error, δLST_A is the atmospheric error, and δLST_N is the error associated with measurement noise. These errors are assumed to be independent.

To calculate the separate contributions from each of these errors let us first denote the simulated atmospheric parameters as $x = [\tau_\lambda(\theta), L_\lambda^\uparrow(\theta), L_\lambda^\downarrow(\theta)]$ and simulated observed radiance parameter as $y = L_\lambda(\theta)$. Both x and y are required to estimate the surface radiance. In reality, however, the input parameters x are not known explicitly, but are associated with some error, δx , which we write as $\hat{x} = x + \delta x$. Similarly, the observed radiances have an associated noise based on the NE Δ T of the specific sensor, which we will denote by \hat{y} . To characterize the model error, we express the retrieval algorithm as a function based on perfect input parameters x and y such that $LST_{TES} = f(x, y)$. The model error, δLST_M , can then be written as:

$$\delta LST_M = E[(f(x, y) - LST_{sim})^2 | x, y]^{1/2} \quad (15)$$

where LST_{sim} is the simulated LST used in the MODTRAN simulations, and $E[|x, y|]$ denotes the mean-square error between the retrieved and simulated LST for inputs x and y . The atmospheric error can be written as the difference between single-band inversion using perfect atmospheric inputs, x and imperfect inputs, \hat{x} :

$$\delta LST_A = E \left[(f(\hat{x}, y) - f(x, y))^2 | x, y \right]^{1/2} \quad (16)$$

And lastly the error due to measurement noise can be written as the difference between single-band inversion with perfect simulated TOA radiances, y and TES with noisy radiances, \hat{y} :

$$\delta LST_N = E \left[(f(x, \hat{y}) - f(x, y))^2 | x, y \right]^{1/2} \quad (17)$$

5.7 Parameterization of Uncertainties

A key requirement for generating an LST ESDR from either multiple sensors or algorithms is accurate knowledge of uncertainties from the contributing products. Uncertainties for each input product must be rigorously estimated for a variety of different conditions on a pixel-by-pixel basis before they can be merged and incorporated into a time series of measurements of sufficient length, consistency, and continuity to adequately meet the science requirements of an ESDR. Current LST&E datasets are available with quality control information, but do not include a full set of uncertainty statistics. For example, the standard ASTER and MODIS LST product QC data planes specify qualitative uncertainty information, and MODIS includes a rough estimate of LST error, but no uncertainty data-planes exist on a pixel-by-pixel basis dependent upon factors such as land cover type, view angle, and total column water vapor.

The next logical step is to apply the uncertainty statistics produced from the TEUSim to real data from GEO-LST retrievals. To achieve this the total uncertainty, taken as the RMSE of the differences between simulated (truth) and retrieved LST including atmospheric error, was modeled according to view angle (SVA), and total water vapor column amount (TCW) using a least-squares method fit to a quadratic function.

$$\delta LST_{GOES} = a_0 + a_1 TCW + a_2 SVA + a_3 TCW \cdot SVA + a_4 TCW^2 + a_5 SVA^2 \quad (18)$$

where δLST is the LST uncertainty (K) calculated as the difference between the simulated and retrieved LST, and a_i are the LST and emissivity regression coefficients.

A sensitivity study showed that the parameterizations given by equations 10–13 provided the best fit to the simulation results in terms of RMSE, with fits of ~ 0.1 K. Once the coefficients are established they can be applied on a pixel-by-pixel basis across any scene given estimates of TCW from either a retrieval (e.g., from MERRA-2), and the *SVA* from the product metadata.

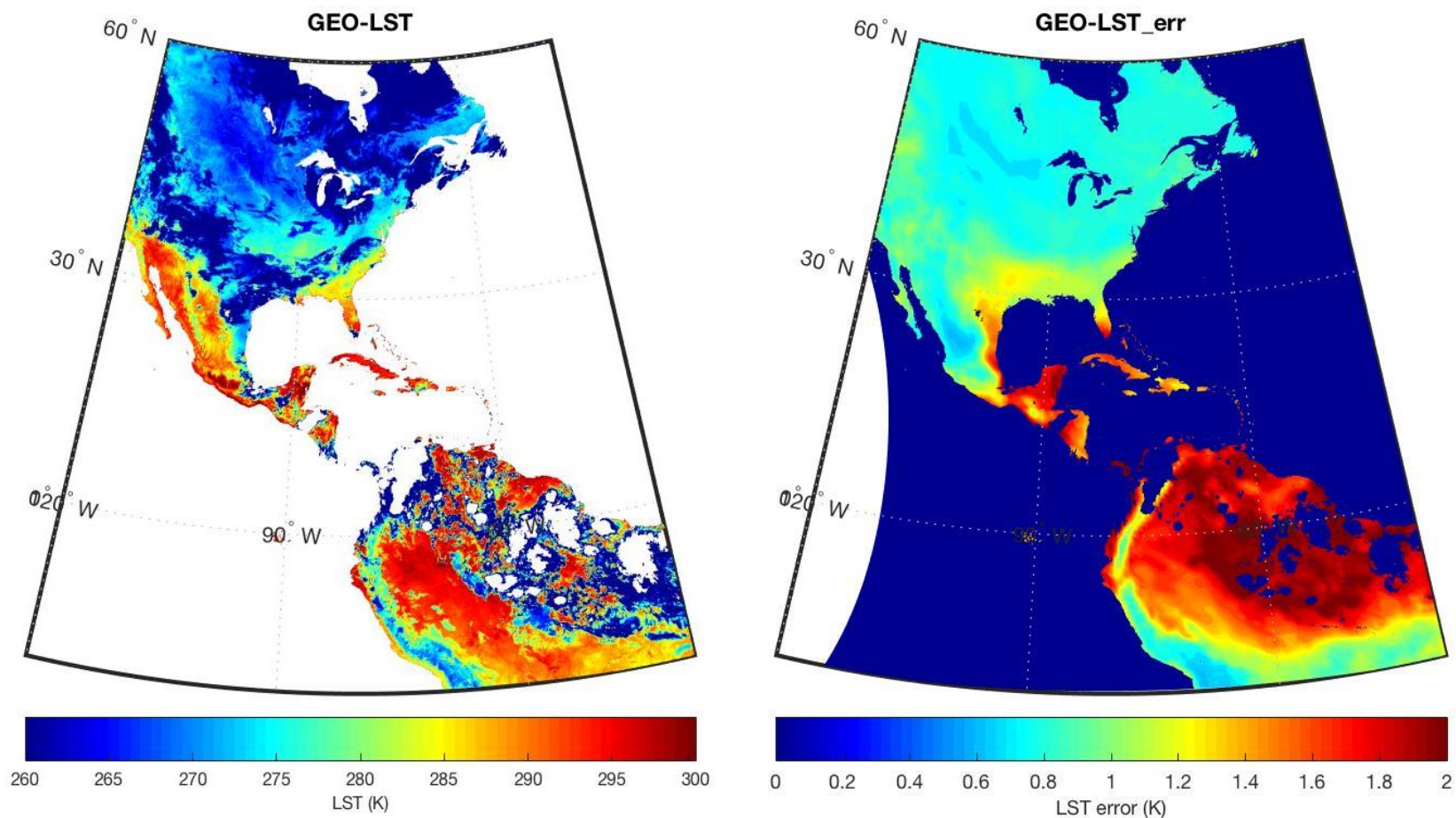


Figure 3: Cloud-masked land surface temperature (left) along with the associated uncertainty (right).

6 Validation

The GEO-LST data have been validated against the MOD11 Version 6 LST product, and against ground data (Pinker et al, 2019). The MODIS LST data products are produced as a series of nine products. The sequence begins as a swath at a nominal pixel spatial resolution of 1 km at nadir and a nominal swath coverage of 2030 or 2040 lines along track by 1354 pixels per line in the daily LST product (Collection-6 MODIS Land Surface Temperature Products Users' Guide, Z. Wan ERI, University of California, Santa Barbara, 2013) (DOI: 10.5067/MODIS/MOD11_L2.006). There are two algorithms used in the daily MODIS LST processing: the generalized split-window LST algorithm (Wan and Dozier, 1996) and the day/night LST algorithm. New refinements made to these two algorithms are described in (Wang, 2014). The MOD11_L2 version 6 swath product provides per-pixel land surface temperature (LST) and emissivity. It is produced daily in 5-minute temporal increments of satellite acquisition and has a pixel size of 1 km. The MOD11C3 Version 6 product provides monthly land surface temperature (LST) and emissivity values in a 0.05 (5600 m x 5600 m) degree latitude/longitude climate modeling grid (CMG), which has a Geographic grid with 7200 columns and 3600 rows representing the entire globe. The MOD11C3 granule consists of day and night LST and their corresponding quality indicator (QC) layers.

NOAA established the Surface Radiation Budget Network (SURFRAD) in 1993 [40] to support climate research by providing accurate, continuous, long-term measurements of the surface radiation budget over the United States. These became the continental U.S. contingent of the International Baseline Surface Radiation Network (BSRN) [41] as described in [42]; the general information about the instrumentation strategy can be found at: <https://www.esrl.noaa.gov/gmd/grad/surfrad/overview.html>. Specifically, we used the following sites: Desert Rock, Nevada (DRA: 36.62° N, 116.02° W); Fort Peck, Montana (FPK: 48.32° N, 105.10° W); Bondville, Illinois (BON: 40.06° N, 88.37° W) and Goodwin Creek, Mississippi (GCM: 34.25° N, 89.87° W). BSRN sites provide data at 1 - or 3-min frequency, which makes them suitable for generating information that matches well the satellite observations.

A homogeneous six-year product of LST at 0.05° spatial resolution at hourly time scale was produced with the record of GOES observations and evaluated for the period of 2004-2009. A six-year climatology at monthly time scales was also derived and used to construct representative diurnal cycles for selected surface type.

The results show that there is a close agreement between the GEO and MOD11 products (see Figure 4; Pinker et al., 2019). The averaged correlation coefficient between them is over 0.9. The averaged difference is less than 2 K and the averaged discrepancy is less than 3.5 K. It was also found that the derived LST has very close correlation with ground-based observations (see Figure 5; Pinker et al., 2019). In most cases, the correlation coefficients are greater than 0.9. The mean bias between the satellite LST and the station LST are less than 1% and over 80% of the bias falls within 1 std. The performance of retrieved LST for daytime and nighttime are comparable to each other. It was also demonstrated that the derived LSTs are of known quality and can be used for a wide range of applications that require a realistic representation of the diurnal cycle.

7 Acknowledgements

The authors would like to thank W. Chen, Y. Ma, and G. Halverson for their contributions towards this work. The research described in this paper was carried out at the Jet Propulsion Laboratory, California Institute of Technology, under contract with the National Aeronautics and Space Administration. © 2019 California Institute of Technology. Government sponsorship acknowledged.

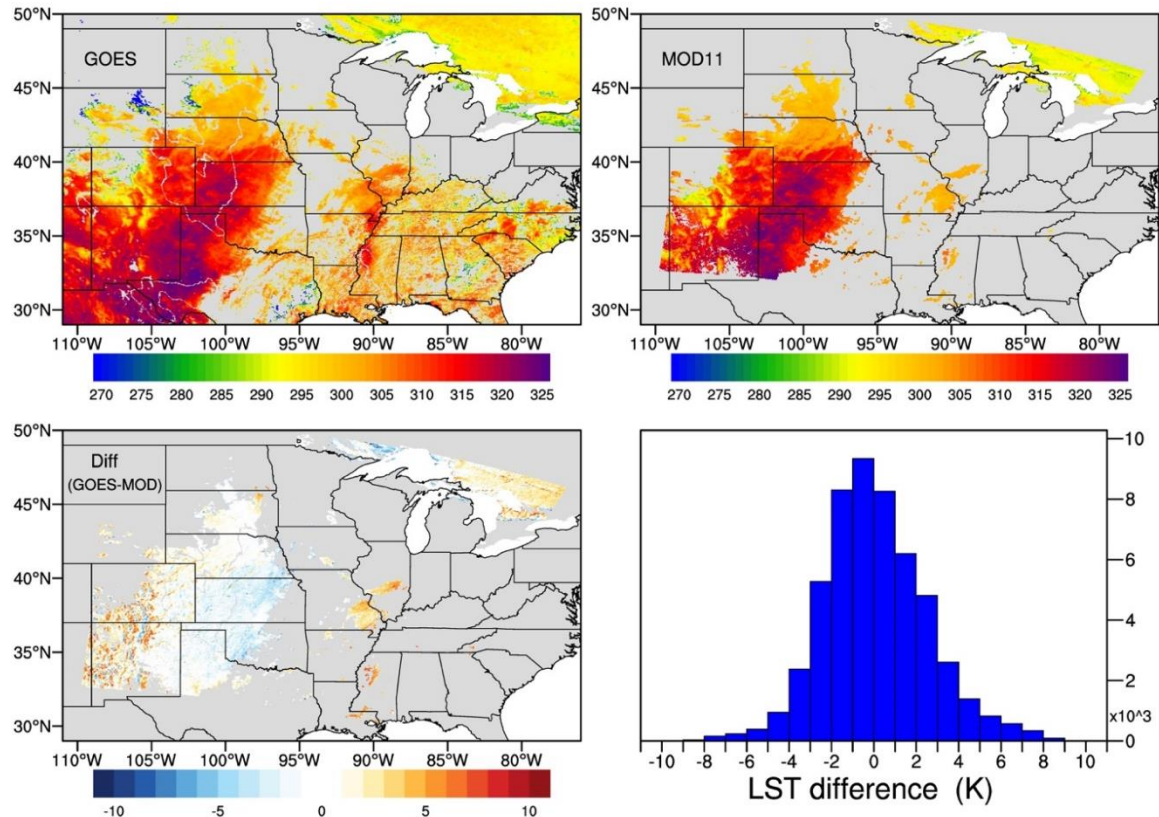


Figure 4. Example case of GOES_RTTOV_LST, MOD11_L2 LST and their difference and its distribution at June, 11 2004 UTC 17:15. (Pinker et al., 2019).

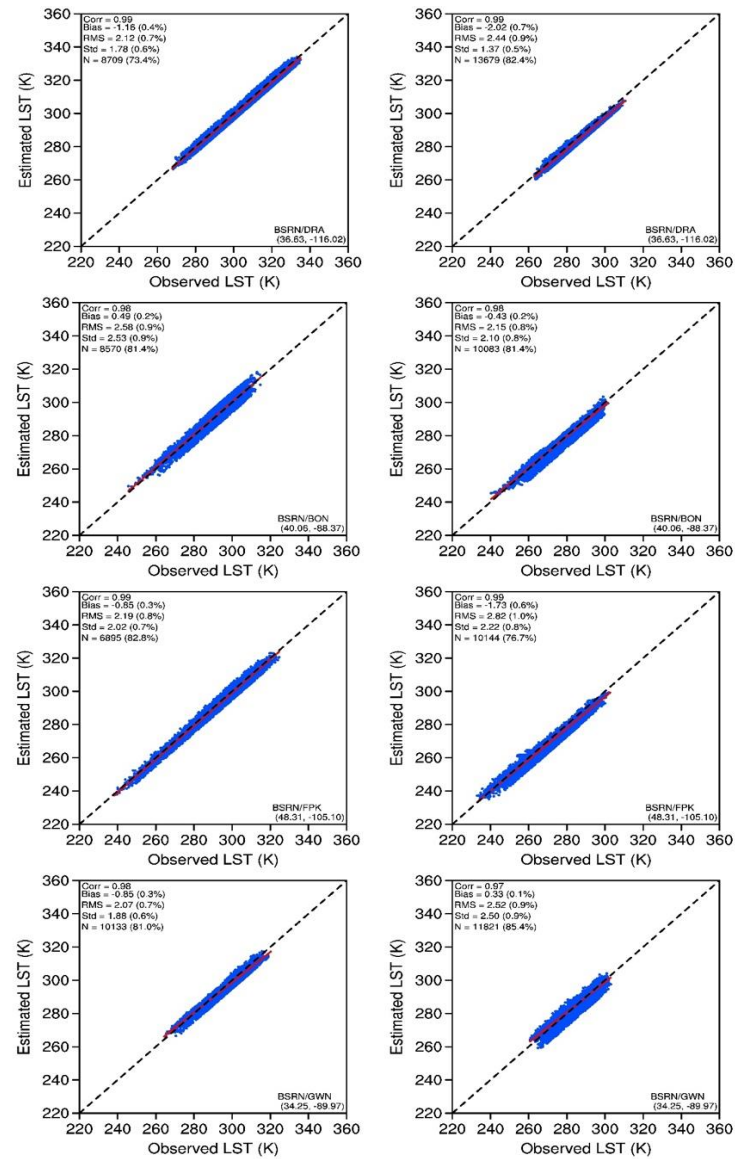


Figure 5. Evaluation of instantaneous GOES based LST estimates at hourly intervals against 4 SURFRAD/BSRN stations, independently for daytime (left panel) and nighttime (right panel) using observations from 2004-2009. (Pinker et al., 2019)

8 References

- Abdalati, W., & Steffen, K. (2001). Greenland ice sheet melt extent: 1979-1999. *Journal of Geophysical Research-Atmospheres*, *106*, 33983-33988
- Anderson, M.C., Hain, C.R., Wardlow, B., Mecikalski, J.R., & Kustas, W.P. (2011a). Evaluation of a drought index based on thermal remote sensing of evapotranspiration over the continental U.S. *Journal of Climate*, *24*, 2025-2044
- Anderson, M.C., Kustas, W.P., Norman, J.M., Hain, C.R., Mecikalski, J.R., Schultz, L., Gonzalez-Dugo, M.P., Cammalleri, C., d'Urso, G., Pimstein, A., & Gao, F. (2011b). Mapping daily evapotranspiration at field to continental scales using geostationary and polar orbiting satellite imagery. *Hydrology and Earth System Sciences*, *15*, 223-239
- Augustine, J.A., DeLuisi, J.J., & Long, C.N. (2000). SURFRAD - A national surface radiation budget network for atmospheric research. *Bulletin of the American Meteorological Society*, *81*, 2341-2357
- Baldrige, A.M., Hook, S.J., Grove, C.I., & Rivera, G. (2009a). The ASTER Spectral Library Version 2.0. *Remote Sensing of Environment*, *114*, 711-715
- Baldrige, A.M., Hook, S.J., Grove, C.I., & Rivera, G. (2009b). The ASTER spectral library version 2.0. *Remote Sensing of Environment*, *113*, 711-715
- Bannari, A., Omari, K., Teillet, R.A., & Fedosejevs, G. (2005). Potential of getis statistics to characterize the radiometric uniformity and stability of test sites used for the calibration of earth observation sensors. *Ieee Transactions on Geoscience and Remote Sensing*, *43*, 2918-2926
- Barducci, A., & Pippi, I. (1996). Temperature and emissivity retrieval from remotely sensed images using the "grey body emissivity" method. *Ieee Transactions on Geoscience and Remote Sensing*, *34*, 681-695
- Barnes, W.L., Pagano, T.S., & Salomonson, V.V. (1998). Prelaunch characteristics of the Moderate Resolution Imaging Spectroradiometer (MODIS) on EOS-AM1. *Ieee Transactions on Geoscience and Remote Sensing*, *36*, 1088-1100
- Barton, I.J., Zavody, A.M., O'Brien, D.M., Cutten, D.R., Saunders, R.W., & Llewellyn-Jones, D.T. (1989). Theoretical Algorithms for Satellite-Derived Sea-Surface Temperatures. *Journal of Geophysical Research-Atmospheres*, *94*, 3365-3375
- Becker, F., & Li, Z.L. (1990). Temperature-Independent Spectral Indexes in Thermal Infrared Bands. *Remote Sensing of Environment*, *32*, 17-33
- Benson, C.S. (1996). Stratigraphic studies in the snow and firn of the Greenland ice sheet, Snow, Ice and Permafrost Research Establishment (now U.S. Army Cold Regions Research and Engineering Laboratory). In
- Berk, A., Anderson, G.P., Acharya, P.K., Bernstein, L.S., Muratov, L., Lee, J., Fox, M., Adler-Golden, S.M., Chetwynd, J.H., Hoke, M.L., Lockwood, R.B., Gardner, J.A., Cooley, T.W., Borel, C.C., & Lewis, P.E. (2005). MODTRANTM 5, A Reformulated Atmospheric Band Model with Auxiliary Species and Practical Multiple Scattering Options: Update. In S.S. Sylvia & P.E. Lewis (Eds.), in *Proc SPIE, Algorithms and Technologies for Multispectral, Hyperspectral, and Ultraspectral Imagery XI* (pp. 662-667). Bellingham, WA: Proceedings of SPIE

- Bonan, G.B., Oleson, K.W., Vertenstein, M., Levis, S., Zeng, X.B., Dai, Y.J., Dickinson, R.E., & Yang, Z.L. (2002). The land surface climatology of the community land model coupled to the NCAR community climate model. *Journal of Climate*, 15, 3123-3149
- Borbas, E., Knuteson, R., Seemann, S.W., Weisz, E., Moy, L., & Huang, H. (2007). A high spectral resolution global land surface infrared emissivity database. In, *Joint 2007 EUMETSAT Meteorological Satellite & 15th AMS Satellite Meteorology and Oceanography Conference*. Amsterdam, The Netherlands
- Bosilovich, M.G., Chen, J.Y., Robertson, F.R., & Adler, R.F. (2008). Evaluation of global precipitation in reanalyses. *Journal of Applied Meteorology and Climatology*, 47, 2279-2299
- Brown, O., & Minnett, P. (1999). MODIS infrared sea surface temperature algorithm. *Algorithm Theoretical Basis Document Version 2*, Univ. of Miami, Miami, Fla.
- Coll, C., & Caselles, V. (1997). A split-window algorithm for land surface temperature from advanced very high resolution radiometer data: Validation and algorithm comparison. *Journal of Geophysical Research-Atmospheres*, 102, 16697-16713
- Coll, C., Caselles, V., Galve, J.M., Valor, E., Niclos, R., Sanchez, J.M., & Rivas, R. (2005). Ground measurements for the validation of land surface temperatures derived from AATSR and MODIS data. *Remote Sensing of Environment*, 97, 288-300
- Coll, C., Caselles, V., Valor, E., Niclos, R., Sanchez, J.M., Galve, J.M., & Mira, M. (2007). Temperature and emissivity separation from ASTER data for low spectral contrast surfaces. *Remote Sensing of Environment*, 110, 162-175
- Coll, C., Wan, Z.M., & Galve, J.M. (2009a). Temperature-based and radiance-based validations of the V5 MODIS land surface temperature product. *Journal of Geophysical Research-Atmospheres*, 114, -
- Coll, C., Wan, Z.M., & Galve, J.M. (2009b). Temperature-based and radiance-based validations of the V5 MODIS land surface temperature product. *Journal of Geophysical Research-Atmospheres*, 114, D20102, doi:20110.21029/22009JD012038
- Comiso, J.C. (2006). Arctic warming signals from satellite observations. *Weather*, 61, 70-76
- Cosnefroy, H.N., Leroy, M., & Briottet, X. (1996). Selection and characterization of Saharan and Arabian desert sites for the calibration of optical satellite sensors. *Remote Sensing of Environment*, 58, 101-114
- de Vries, C., Danaher, T., Denham, R., Scarth, P., & Phinn, S. (2007). An operational radiometric calibration procedure for the Landsat sensors based on pseudo-invariant target sites. *Remote Sensing of Environment*, 107, 414-429
- Deschamps, P.Y., & Phulpin, T. (1980). Atmospheric Correction of Infrared Measurements of Sea-Surface Temperature Using Channels at 3.7, 11 and 12 μ -M. *Boundary-Layer Meteorology*, 18, 131-143
- Dousset, B., & Gourmelon, F. (2003). Satellite multi-sensor data analysis of urban surface temperatures and landcover. *Ispr Journal of Photogrammetry and Remote Sensing*, 58, 43-54
- Dousset, B., Gourmelon, F., Laaidi, K., Zeghnoun, A., Giraudet, E., Bretin, P., Mauri, E., & Vandentorren, S. (2011). Satellite monitoring of summer heat waves in the Paris metropolitan area. *International Journal of Climatology*, 31, 313-323

- Eyre, J.R., & Woolf, H.M. (1988). Transmittance of Atmospheric Gases in the Microwave Region - a Fast Model. *Applied Optics*, 27, 3244-3249
- Francois, C., Brisson, A., Le Borgne, P., & Marsouin, A. (2002). Definition of a radiosounding database for sea surface brightness temperature simulations - Application to sea surface temperature retrieval algorithm determination. *Remote Sensing of Environment*, 81, 309-326
- Francois, C., & Otle, C. (1996). Atmospheric corrections in the thermal infrared: Global and water vapor dependent Split-Window algorithms - Applications to ATSR and AVHRR data. *Ieee Transactions on Geoscience and Remote Sensing*, 34, 457-470
- French, A.N., Schmugge, T.J., Ritchie, J.C., Hsu, A., Jacob, F., & Ogawa, K. (2008). Detecting land cover change at the Jornada Experimental Range, New Mexico with ASTER emissivities. *Remote Sensing of Environment*, 112, 1730-1748
- Galve, J.A., Coll, C., Caselles, V., & Valor, E. (2008). An atmospheric radiosounding database for generating land surface temperature algorithms. *Ieee Transactions on Geoscience and Remote Sensing*, 46, 1547-1557
- Gillespie, A., Rokugawa, S., Hook, S., Matsunaga, T., & Kahle, A.B. (1999). Temperature/Emissivity Separation Algorithm Theoretical Basis Document, Version 2.4, ASTER TES ATBD, NASA Contract NAS5-31372, 31322 March, 31999
- Gillespie, A., Rokugawa, S., Matsunaga, T., Cothorn, J.S., Hook, S., & Kahle, A.B. (1998). A temperature and emissivity separation algorithm for Advanced Spaceborne Thermal Emission and Reflection Radiometer (ASTER) images. *Ieee Transactions on Geoscience and Remote Sensing*, 36, 1113-1126
- Gottsche, F.M., & Hulley, G.C. (2012). Validation of six satellite-retrieved land surface emissivity products over two land cover types in a hyper-arid region. *Remote Sensing of Environment*, 124, 149-158
- Gustafson, W.T., Gillespie, A.R., & Yamada, G.J. (2006). Revisions to the ASTER temperature/emissivity separation algorithm. In *2nd International Symposium on Recent Advances in Quantitative Remote Sensing*. Torrent (Valencia), Spain
- Hall, D.K., Williams Jr., R.S., Casey, K.A., Digirolamo, N.E., & Wan, Z. (2006). Satellite-derived, melt-season surface temperature of the Greenland Ice Sheet (2000-2005) and its relationship to mass balance. *Geophysical Research Letters*, 33:L11501, doi:10.1029/2006GL026444
- Hall, D.K., Williams, R.S., Luthcke, S.B., & Digirolamo, N.E. (2008). Greenland ice sheet surface temperature, melt and mass loss: 2000-06. *Journal of Glaciology*, 54, 81-93
- Hall, D.K., Comiso, J.C., DiGirolamo, N.E., Shuman, C.A., Key, J.R., & Koenig, L.S. (2012). A Satellite-Derived Climate-Quality Data Record of the Clear-Sky Surface Temperature of the Greenland Ice Sheet. *Journal of Climate*, 25, 4785-4798
- Hain, C.R., Crow, W.T., Mecikalski, J.R., Anderson, M.C., & Holmes, T. (2011). An intercomparison of available soil moisture estimates from thermal infrared and passive microwave remote sensing and land surface modeling. *Journal of Geophysical Research-Atmospheres*, 116
- Hook, S., Johnson, W., & Abrams, M. (2013). NASA's Hyperspectral Thermal Emission Spectrometer (HyTES). In C. Kuenzer & S. Dech (Eds.), *Thermal Infrared Remote Sensing - Sensors, Methods, Applications*: Springer

- Hook, S.J., Dmochowski, J.E., Howard, K.A., Rowan, L.C., Karlstrom, K.E., & Stock, J.M. (2005). Mapping variations in weight percent silica measured from multispectral thermal infrared imagery - Examples from the Hiller Mountains, Nevada, USA and Tres Virgenes-La Reforma, Baja California Sur, Mexico. *Remote Sensing of Environment*, 95, 273-289
- Hook, S.J., Gabell, A.R., Green, A.A., & Kealy, P.S. (1992). A Comparison of Techniques for Extracting Emissivity Information from Thermal Infrared Data for Geologic Studies. *Remote Sensing of Environment*, 42, 123-135
- Hook, S.J., Vaughan, R.G., Tonooka, H., & Schladow, S.G. (2007). Absolute radiometric in-flight validation of mid infrared and thermal infrared data from ASTER and MODIS on the terra spacecraft using the Lake Tahoe, CA/NV, USA, automated validation site. *Ieee Transactions on Geoscience and Remote Sensing*, 45, 1798-1807
- Hulley, G.C., & Hook, S.J. (2009a). Intercomparison of Versions 4, 4.1 and 5 of the MODIS Land Surface Temperature and Emissivity Products and Validation with Laboratory Measurements of Sand Samples from the Namib Desert, Namibia. *Remote Sensing of Environment*, 113, 1313-1318
- Hulley, G.C., Hook, S.J., & Baldrige, A.M. (2008). ASTER land surface emissivity database of California and Nevada. *Geophysical Research Letters*, 35, L13401, doi: 13410.11029/12008gl034507
- Hulley, G.C., Hook, S.J., & Baldrige, A.M. (2009a). Validation of the North American ASTER Land Surface Emissivity Database (NAALSED) version 2.0 using pseudo-invariant sand dune sites. *Remote Sensing of Environment*, 113, 2224-2233
- Hulley, G.C., & Hook, S.J. (2009b). The North American ASTER Land Surface Emissivity Database (NAALSED) Version 2.0. *Remote Sensing of Environment*, 1967-1975
- Hulley, G.C., Hook, S.J., Manning, E., Lee, S.Y., & Fetzer, E.J. (2009c). Validation of the Atmospheric Infrared Sounder (AIRS) Version 5 (v5) Land Surface Emissivity Product over the Namib and Kalahari Deserts. *Journal of Geophysical Research Atmospheres*, 114, D19104
- Hulley, G.C., Hook, S.J., & Baldrige, A.M. (2010). Investigating the Effects of Soil Moisture on Thermal Infrared Land Surface Temperature and Emissivity Using Satellite Retrievals and Laboratory Measurements. *Remote Sensing of Environment*, 114, 1480-1493
- Hulley, G.C., & Hook, S.J. (2011). Generating Consistent Land Surface Temperature and Emissivity Products Between ASTER and MODIS Data for Earth Science Research. *Ieee Transactions on Geoscience and Remote Sensing*, 49, 1304-1315
- Hulley, G.C., & Hook, S.J. (2012). A radiance-based method for estimating uncertainties in the Atmospheric Infrared Sounder (AIRS) land surface temperature product. *Journal of Geophysical Research-Atmospheres*, 117
- Hulley, G.C., Hughes, T., & Hook, S.J. (2012). Quantifying Uncertainties in Land Surface Temperature (LST) and Emissivity Retrievals from ASTER and MODIS Thermal Infrared Data. *Journal of Geophysical Research Atmospheres*, 117, D23.
- Hulley, G., Veraverbeke, S., & Hook, S. (2014). Thermal-based techniques for land cover change detection using a new dynamic MODIS multispectral emissivity product (MOD21). *Remote Sensing of Environment*, 140, 755-765

- Hulley, G.C., Hook, S.J., Abbott, E., Malakar, N., Islam, T., & Abrams, M. (2015a). The ASTER Global Emissivity Database (ASTER GED): Mapping Earth's emissivity at 100 meter spatial scale. *Geophysical Research Letters*, 42, doi:10.1002/2015GL065564
- Hulley, G.C., Hook, S.J., Abbott, E., Malakar, N., Islam, T., & Abrams, M. (2015b). The ASTER Global Emissivity Dataset (ASTER GED): Mapping Earth's emissivity at 100 meter spatial scale. *Geophysical Research Letters*, 42, 7966-7976
- Hulley, G., Malakar, N., Freepartner, R. (2016). Moderate Resolution Imaging Spectroradiometer (MODIS) Land Surface Temperature and Emissivity Product (MxD21) Algorithm Theoretical Basis Document Collection-6. Revision 2.4, Jet Propulsion Laboratory, Pasadena, CA, 2016.
- Jimenez-Munoz, J.C., & Sobrino, J.A. (2010). A Single-Channel Algorithm for Land-Surface Temperature Retrieval From ASTER Data. *Ieee Geoscience and Remote Sensing Letters*, 7, 176-179
- Jin, M.L., & Liang, S.L. (2006). An improved land surface emissivity parameter for land surface models using global remote sensing observations. *Journal of Climate*, 19, 2867-2881
- Justice, C., & Townshend, J. (2002). Special issue on the moderate resolution imaging spectroradiometer (MODIS): a new generation of land surface monitoring. *Remote Sensing of Environment*, 83, 1-2
- Justice, C.O., Vermote, E., Townshend, J.R.G., Defries, R., Roy, D.P., Hall, D.K., Salomonson, V.V., Privette, J.L., Riggs, G., Strahler, A., Lucht, W., Myneni, R.B., Knyazikhin, Y., Running, S.W., Nemani, R.R., Wan, Z.M., Huete, A.R., van Leeuwen, W., Wolfe, R.E., Giglio, L., Muller, J.P., Lewis, P., & Barnsley, M.J. (1998). The Moderate Resolution Imaging Spectroradiometer (MODIS): Land remote sensing for global change research. *Ieee Transactions on Geoscience and Remote Sensing*, 36, 1228-1249
- Kalnay, E., Kanamitsu, M., & Baker, W.E. (1990). Global Numerical Weather Prediction at the National-Meteorological-Center. *Bulletin of the American Meteorological Society*, 71, 1410-1428
- Kealy, M.J., Montgomery, M., & Dovidio, J.F. (1990). Reliability and Predictive-Validity of Contingent Values - Does the Nature of the Good Matter. *Journal of Environmental Economics and Management*, 19, 244-263
- Kealy, P.S., & Hook, S. (1993). Separating temperature & emissivity in thermal infrared multispectral scanner data: Implication for recovering land surface temperatures. *Ieee Transactions on Geoscience and Remote Sensing*, 31, 1155-1164
- Key, J.R., Mahoney, R., Liu, Y.H., Romanov, P., Tschudi, M., Appel, I., Maslanik, J., Baldwin, D., Wang, X.J., & Meade, P. (2013). Snow and ice products from Suomi NPP VIIRS. *Journal of Geophysical Research-Atmospheres*, 118, 12816-12830
- Kinter, J.L., Shukla, J., Marx, L., & Schneider, E.K. (1988). A simulation of the winter and summer circulations with the NMC global spectral model. *Journal of Atmospheric Science*, 45, 2486-2522
- Kneizys, F.X., Abreu, L.W., Anderson, G.P., Chetwynd, J.H., Shettle, E.P., Berk, A., Bernstein, L.S., Robertson, D.C., Acharya, P.K., Rothman, L.A., Selby, J.E.A., Gallery, W.O., & Clough, S.A. (1996). The MODTRAN 2/3 Report & LOWTRAN 7 Model, F19628-91-C-0132. In, *Phillips Lab. Hanscom AFB, MA*

- Li, F.Q., Jackson, T.J., Kustas, W.P., Schmugge, T.J., French, A.N., Cosh, M.H., & Bindlish, R. (2004). Deriving land surface temperature from Landsat 5 and 7 during SMEX02/SMACEX. *Remote Sensing of Environment*, 92, 521-534
- Li, Z.L., Becker, F., Stoll, M.P., & Wan, Z.M. (1999). Evaluation of six methods for extracting relative emissivity spectra from thermal infrared images. *Remote Sensing of Environment*, 69, 197-214
- Luvall, J., Quattrochi, D.A., Rickman, D., & Estes, M.G. (Eds.) (2015). Urban Heat Islands: Encyclopedia of Atmospheric Sciences
- Lyon, R. (1965). Analysis of ROcks by Spectral INfrared Emission (8 to 25 microns). *Economic Geology and the Bulletin of the Society of Economic Geologists*, 60, 715-736
- Malakar, N.K., & Hulley, G.C. (2016). A Water Vapor Scaling Model for Improved Land Surface Temperature and Emissivity Separation of MODIS Thermal Infrared Data. *Remote Sensing of Environment*, 182, 252-264.
- Malakar, N.K., G. C. Hulley, S. J. Hook, K. Laraby, M. Cook and J. R. Schott. (2018). An Operational Land Surface Temperature Product for Landsat Thermal Data: Methodology and Validation. *IEEE Transactions on Geoscience and Remote Sensing*, 56(10), 5717-5735.
- Masuda, K., Takashima, T., & Takayama, Y. (1988). Emissivity of Pure and Sea Waters for the Model Sea-Surface in the Infrared Window Regions. *Remote Sensing of Environment*, 24, 313-329
- Matricardi, M. (2009). Technical Note: An assessment of the accuracy of the RTTOV fast radiative transfer model using IASI data. *Atmospheric Chemistry and Physics*, 9, 6899-6913
- Matricardi, M., Chevallier, F., & Tjemkes, S.A. (2001). An improved general fast radiative transfer model for the assimilation of radiance observations. In: European Centre for Medium-Range Weather Forecasts
- Matsunaga, T. (1994). A temperature-emissivity separation method using an empirical relationship between the mean, the maximum, & the minimum of the thermal infrared emissivity spectrum, in Japanese with English abstract. *Journal Remote Sensing Society Japan*, 14, 230-241
- Mira, M., Valor, E., Boluda, R., Caselles, V., & Coll, C. (2007). Influence of soil water content on the thermal infrared emissivity of bare soils: Implication for land surface temperature determination. *Journal of Geophysical Research-Earth Surface*, 112, F04003
- Mushkin, A., & Gillespie, A.R. (2005). Estimating sub-pixel surface roughness using remotely sensed stereoscopic data. *Remote Sensing of Environment*, 99, 75-83
- NASA (2005). Exploring our Planet for the Benefit of Society, NASA Earth Science and Applications from Space, Strategic Roadmap, http://images.spaceref.com/news/2005/earth_roadmap.pdf
- NASA (2011). NASA Earth Science Data Records Programs, http://science.nasa.gov/earth-science/earth-science-data/Earth-Science-Data-Records-Programs/#ESDR_uncertainty_analysis
- Norman, J.M., & Becker, F. (1995). Terminology in Thermal Infrared Remote-Sensing of Natural Surfaces. *Agricultural and Forest Meteorology*, 77, 153-166
- Ogawa, K. (2004). Mapping Surface Broadband Emissivity of the Sahara Desert Using ASTER and MODIS Data. *Earth Interactions*, 8, -

- Ogawa, K., Schmugge, T., Jacob, F., & French, A. (2003). Estimation of land surface window (8-12 μ m) emissivity from multispectral thermal infrared remote sensing - A case study in a part of Sahara Desert. *Geophysical Research Letters*, 30, -
- Ogawa, K., Schmugge, T., & Rokugawa, S. (2006). Observations of the dependence of the thermal infrared emissivity on soil moisture. *Geophysical Research Abstracts*, 8, 04996
- Oleson, K.W., Bonan, G.B., Levis, S., & Vertenstein, M. (2004). Effects of land use change on North American climate: impact of surface datasets and model biogeophysics. *Climate Dynamics*, 23, 117-132
- Palluconi, F., Hoover, G., Alley, R.E., Nilsen, M.J., & Thompson, T. (1999). An atmospheric correction method for ASTER thermal radiometry over land, ASTER algorithm theoretical basis document (ATBD), Revision 3, Jet Propulsion Laboratory, Pasadena, CA, 1999
- Parkinson, C.L., Cavalieri, D.J., Gloersen, P., Zwally, H.J., & Comiso, J.C. (1999). Arctic sea ice extents, areas, and trends, 1978-1996. *Journal of Geophysical Research-Oceans*, 104, 20837-20856
- Pinker, R.T.; Ma, Y.; Chen, W.; Hulley, G.; Borbas, E.; Islam, T.; Hain, C.; Cawse-Nicholson, K.; Hook, S.; Basara, J. (2019). Towards a Unified and Coherent Land Surface Temperature Earth System Data Record from Geostationary Satellites. *Remote Sensing*, 11, 1399.
- Prata, A.J. (1994). Land-Surface Temperatures Derived from the Advanced Very High-Resolution Radiometer and the Along-Track Scanning Radiometer .2. Experimental Results and Validation of Avhrr Algorithms. *Journal of Geophysical Research-Atmospheres*, 99, 13025-13058
- Price, J.C. (1984). Land surface temperature measurements from the split window channels of the NOAA 7 Advanced Very High Resolution Radiometer. *Journal of Geophysical Research*, 89, 7231-7237
- Rhee, J., Im, J., & Carbone, G.J. (2010). Monitoring agricultural drought for arid and humid regions using multi-sensor remote sensing data. *Remote Sensing of Environment*, 114, 2875-2887
- Sabol, D.E., Gillespie, A.R., Abbott, E., & Yamada, G. (2009). Field validation of the ASTER Temperature-Emissivity Separation algorithm. *Remote Sensing of Environment*, 113, 2328-2344
- Salomonson, V.V., Barnes, W.L., Maymon, P.W., Montgomery, H.E., & Ostrow, H. (1989). Modis - Advanced Facility Instrument for Studies of the Earth as a System. *Ieee Transactions on Geoscience and Remote Sensing*, 27, 145-153
- Saunders, R., Matricardi, M., & Brunel, P. (1999). An improved fast radiative transfer model for assimilation of satellite radiance observations. *Quarterly Journal of the Royal Meteorological Society*, 125, 1407-1425
- Schneider, P., & Hook, S.J. (2010). Space observations of inland water bodies show rapid surface warming since 1985. *Geophysical Research Letters*, 37
- Seemann, S.W., Borbas, E., Li, J., Menzel, P., & Gumley, L.E. (2006). MODIS Atmospheric Profile Retrieval Algorithm Theoretical Basis Document, Cooperative Institute for Meteorological Satellite Studies, University of Wisconsin-Madison, Madison, WI, Version 6, October 25, 2006
- Seemann, S.W., Borbas, E.E., Knuteson, R.O., Stephenson, G.R., & Huang, H.L. (2008). Development of a global infrared land surface emissivity database for application to clear sky

- sounding retrievals from multispectral satellite radiance measurements. *Journal of Applied Meteorology and Climatology*, 47, 108-123
- Seemann, S.W., Li, J., Menzel, W.P., & Gumley, L.E. (2003). Operational retrieval of atmospheric temperature, moisture, and ozone from MODIS infrared radiances. *Journal of Applied Meteorology*, 42, 1072-1091
- Semmens, K.A., Anderson, M.C., Kustas, W.P., Gao, F., Alfieri, J.G., McKee, L., Prueger, J.H., Hain, C.R., Cammalleri, C., Yang, Y., Xia, T., Sanchez, L., Alsina, M.M., & Velez, M. (2016). Monitoring daily evapotranspiration over two California vineyards using Landsat 8 in a multi-sensor data fusion approach. *Remote Sensing of Environment*, 185, 155-170
- Snyder, W.C., Wan, Z., Zhang, Y., & Feng, Y.Z. (1998). Classification-based emissivity for land surface temperature measurement from space. *International Journal of Remote Sensing*, 19, 2753-2774
- Snyder, W.C., Wan, Z.M., Zhang, Y.L., & Feng, Y.Z. (1997). Thermal infrared (3-14 μ m) bidirectional reflectance measurements of sands and soils. *Remote Sensing of Environment*, 60, 101-109
- Strahler, A.H., Zhang, X., Cooper, A., Schaaf, C., Friedl, M., Hodges, J., Baccini, A., & Gao, F. (2002). Validation of the consistent-year v003 MODIS land cover product. <http://www-modis.bu.edu/landcover/userguidelc/consistent.htm>
- Susskind, J., Barnet, C.D., & Blaisdell, J.M. (2003). Retrieval of atmospheric and surface parameters from AIRS/AMSU/HSB data in the presence of clouds. *Ieee Transactions on Geoscience and Remote Sensing*, 41, 390-409
- Susskind, J., & Blaisdell, J. (2008). Improved surface parameter retrievals using AIRS/AMSU data. Proc. SPIE, 6966, DOI: 10.1117/1112.774759
- Teillet, P.M., Fedosejevs, G., Gautier, R.P., & Schowengerdt, R.A. (1998). Uniformity characterization of land test sites used for radiometric calibration of earth observation sensors. In, *Proc. 20th Can. Symp. Remote Sensing* (pp. 1-4). Calgary, AB, Canada
- Tobin, D.C., Revercomb, H.E., Knuteson, R.O., Lesht, B.M., Strow, L.L., Hannon, S.E., Feltz, W.F., Moy, L.A., Fetzer, E.J., & Cress, T.S. (2006). Atmospheric Radiation Measurement site atmospheric state best estimates for Atmospheric Infrared Sounder temperature and water vapor retrieval validation. *Journal of Geophysical Research-Atmospheres*, 111, -
- Tonooka, H. (2001). An atmospheric correction algorithm for thermal infrared multispectral data over land - A water-vapor scaling method. *Ieee Transactions on Geoscience and Remote Sensing*, 39, 682-692
- Tonooka, H. (2005). Accurate atmospheric correction of ASTER thermal infrared imagery using the WVS method. *Ieee Transactions on Geoscience and Remote Sensing*, 43, 2778-2792
- Tonooka, H., & Palluconi, F.D. (2005). Validation of ASTER/TIR standard atmospheric correction using water surfaces. *Ieee Transactions on Geoscience and Remote Sensing*, 43, 2769-2777
- Tonooka, H., Palluconi, F.D., Hook, S.J., & Matsunaga, T. (2005). Vicarious calibration of ASTER thermal infrared bands. *Ieee Transactions on Geoscience and Remote Sensing*, 43, 2733-2746

- Valor, E., & Caselles, V. (1996). Mapping land surface emissivity from NDVI: Application to European, African, and South American areas. *Remote Sensing of Environment*, 57, 167-184
- Vargas, M., Miura, T., Shabanov, N., & Kato, A. (2013). An initial assessment of Suomi NPP VIIRS vegetation index EDR. *Journal of Geophysical Research-Atmospheres*, 118, 12301-12316
- Vaughan, R.G., Hook, S.J., Calvin, W.M., & Taranik, J.V. (2005). Surface mineral mapping at Steamboat Springs, Nevada, USA, with multi-wavelength thermal infrared images. *Remote Sensing of Environment*, 99, 140-158
- Wan, Z. (1999). MODIS Land-Surface Temperature Algorithm Theoretical Basis Document (LST ATBD), Version 3.3, University of California, Santa Barbara, April 1999
- Wan, Z., & Li, Z.L. (2008). Radiance-based validation of the V5 MODIS land-surface temperature product. *International Journal of Remote Sensing*, 29, 5373-5395
- Wan, Z., Zhang, Y., Zhang, Q., & Li, Z.L. (2004). Quality assessment and validation of the MODIS global land surface temperature. *International Journal of Remote Sensing*, 25, 261-274
- Wan, Z.M. (2008). New refinements and validation of the MODIS Land-Surface Temperature/Emissivity products. *Remote Sensing of Environment*, 112, 59-74
- Wan, Z.M., & Dozier, J. (1996). A generalized split-window algorithm for retrieving land-surface temperature from space. *Ieee Transactions on Geoscience and Remote Sensing*, 34, 892-905
- Wan, Z.M., & Li, Z.L. (1997). A physics-based algorithm for retrieving land-surface emissivity and temperature from EOS/MODIS data. *Ieee Transactions on Geoscience and Remote Sensing*, 35, 980-996
- Wang, K.C., & Liang, S.L. (2009). Evaluation of ASTER and MODIS land surface temperature and emissivity products using long-term surface longwave radiation observations at SURFRAD sites. *Remote Sensing of Environment*, 113, 1556-1565
- Watson, K. (1992). Spectral Ratio Method for Measuring Emissivity. *Remote Sensing of Environment*, 42, 113-116
- Watson, K., Kruse, F.A., & Hummermilller, S. (1990). Thermal Infrared Exploration in the Carlin Trend, Northern Nevada. *Geophysics*, 55, 70-79
- Yao, Z.G., Li, J., Li, J.L., & Zhang, H. (2011). Surface Emissivity Impact on Temperature and Moisture Soundings from Hyperspectral Infrared Radiance Measurements. *Journal of Applied Meteorology and Climatology*, 50, 1225-1235
- Yu, Y., Pinheiro, J.L., & Privette, J.L. (2006). Correcting Land Surface Temperature Measurements for Directional Emissivity Over 3-D Structured Vegetation. *Proc. SPIE*, 6298, 629817, DOI:629810.621117/629812.682951
- Yu, Y., Privette, J.L., & Pinheiro, A.C. (2008). Evaluation of split-window land surface temperature algorithms for generating climate data records. *Ieee Transactions on Geoscience and Remote Sensing*, 46, 179-192
- Yu, Y.Y., Privette, J.L., & Pinheiro, A.C. (2005). Analysis of the NPOESS VIIRS land surface temperature algorithm using MODIS data. *Ieee Transactions on Geoscience and Remote Sensing*, 43, 2340-2350

Zeng, Q.C., Zhang, X.H., Liang, X.Z., Yuan, C.G., & Chen, S.F. (1989). Documentation of IAP two-level atmospheric general circulation model. In U.S.D.o. Energy (Ed.) (p. 383 pp.). Washington, D.C.

Zhou, L., Dickinson, R.E., Ogawa, K., Tian, Y., Jin, M., Schmugge, T., & Tsvetsinskaya, E. (2003a). Relations between albedos and emissivities from MODIS and ASTER data over North African desert. *Geophysical Research Letters*, 30, -

Zhou, L., Dickinson, R.E., Tian, Y., Jin, M., Ogawa, K., Yu, H., & Schmugge, T. (2003b). A sensitivity study of climate and energy balance simulations with use of satellite-derived emissivity data over Northern Africa and the Arabian Peninsula. *Journal of Geophysical Research-Atmospheres*, 108, 4795
